Supporting Information for

Quantum tailoring for polarization-discriminating Bi_2S_3 nanowire photodetectors and their multiplexing optical communication and imaging applications

Huaxin Yi,[ab#] Churong Ma,[c#] Wan Wang,[a] Huanrong Liang,[a] Rui Cui,[a] Weiwei Cao,[a] Hailin Yang,[a] Yuhang Ma,[a] Wenjing Huang,[d] Zhaoqiang Zheng,[d] Yichao Zou,[a] Zexiang Deng,[e]* Jiandong Yao,[ab]* and Guowei Yang[ab]

[a] State Key Laboratory of Optoelectronic Materials and Technologies, Nanotechnology Research Center, School of Materials Science & Engineering, Sun Yat-sen University, Guangzhou 510275 Guangdong, P. R. China

[b] Guangzhou Key Laboratory of Flexible Electronic Materials and Wearable Devices, Sun Yat-sen University, Guangzhou 510275 Guangdong, P. R. China

[c] Guangdong Provincial Key Laboratory of Optical Fiber Sensing and Communications, Institute of Photonics Technology, Jinan University, Guangzhou 511443 Guangdong, P. R. China

[d] School of Materials and Energy, Guangdong University of Technology, Guangzhou 510006 Guangdong, P. R. China

[e] School of Science, Guilin University of Aerospace Technology, Guilin 541004 Guangxi, P. R. China

[#]These authors contribute equally to this work.

*Authors to whom correspondence should be addressed: dengzex@mail2.sysu.edu.cn

& yaojd3@mail.sysu.edu.cn

Note S1.

APCVD Growth of Monocrystalline Bi_2S_3 Nanowires: High-quality monocrystalline Bi_2S_3 nanowires were synthesized by APCVD in a two-inch-diameter dual-heating-zone tubular furnace (GSL-1100X-S). Specifically, 200 mg of sulfur powder (99.9%, Aladdin) and 10 mg of bismuth (III) sulfide powder (99.9%, Aladdin) were placed as source materials in the center of the upstream zone and downstream zone (with a distance of 25 cm), respectively, and freshly cleaned 1×1 cm mica sheets were placed as the growth substrates, which were approximately 12 cm away from the center of the downstream heating zone. Prior to running the growth program, argon gas (99.99%) with a gas flow rate of 200 sccm was introduced to purge the tube for 30 minutes to remove the impurity gases and moisture, after which the argon gas flow rate was dropped to 30 sccm. Subsequently, the downstream heating zone of the tubular furnace was ramped up to 150 °C within 27 mins. Then, it was further ramped up to 720 °C at a heating rate of 15 °C min^{-1}, where the temperature was maintained for 8 minutes for the deposition of Bi_2S_3 nanowires. After the growth, the furnace was naturally cooled down to room temperature.

Material Characterizations: The morphology of the Bi_2S_3 nanowires was observed through an optical microscope (Nikon ECLIPSE LV100ND). The crystal structure of the Bi_2S_3 nanowires was characterized by X-ray diffraction system (Rigaku D-MAX 2200 VPC). Angle-resolved Raman spectra of the Bi_2S_3 nanowires were measured by a Renishaw in Via Reflex system with an excitation laser of 514 nm. The widths of the Bi_2S_3 nanowires were confirmed by atomic force microscopy (AFM, Bruker Dimension FastScan). The Kelvin probe force microscopy (KPFM) measurement is conducted using the same equipment. The element valance states of the Bi_2S_3 nanowires were tested by a Thermo Scientific XPS system (Nexsa). The UV-Vis-NIR absorption spectrum was measured with a UV-Vis-NIR spectrophotometer (Lambda950, Perkin Elmer). Transmission electron microscopy (TEM) and selected area electron diffraction (SAED, FEITecnaiG2F30) measurements were conducted to explore the microscopic crystal structures of the Bi_2S_3 nanowire. The composition and

proportion of elements were analyzed by scanning electron microscopy (SEM, Hitachi Regulus 8230) equipped with a Bruker Quantax X-ray energy-dispersive spectrometer (EDS). The polarization-resolved optical microscopy images were obtained using a DM2700P system. The refractive index used for simulations is extracted by an ellipsometer (HORIBA UVISEL PLUS).

Device Fabrication: The Bi_2S_3 photodetectors were fabricated by transferring the Bi_2S_3 nanowires grown on mica onto the SiO_2/Si substrates via a PDMS-assisted dry transfer technology. The electrode patterns were defined through maskless ultraviolet photolithography (Heidelberg, μpg 501). Following this, the Ti (10 nm)/Au (100 nm) electrodes were deposited by an e-beam evaporation system (Wavetest, DE400).

Evaluation of the Light-Sensing Properties: The electrical and optoelectronic properties of the Bi_2S_3 photodetectors were measured on a probe station (Lakeshore) equipped with a semiconductor parameter analyzer (PDA FS-Pro) in the ambient condition. Lasers with different wavelengths including 370.6, 405, 532, 635, 808, 1064, 1310 and 1550 nm were used as the light sources to irradiate the devices. The polarization angle-dependent photoresponse is characterized by rotating the half-wave plate in the optical path below the polarizer. Pulsed light signal is generated by a high-speed chopper for characterizing the response rate.

First-Principles Calculations: Based on the density functional theory (DFT), we extracted the strain-dependent electronic band structures by using the Quantum Espresso software, with the strain from –8% to 8%. In the DFT calculation, the ***k***-point grids were set to 5 × 5 × 11 in the optimization and the band structure calculations, with the kinetic energy cutoff of 100 Ry in all calculations. The type of the exchange-correlation functional was the Perdew–Burke–Ernzerhof (PBE) generalized gradient approximation (GGA), based on the ultrasoft pseudopotentials. The convergence of force and electronic energy were set to 0.001 eV/Å and 10^{-8} eV, respectively in all calculations. The energy level of vacuum far from the material is set to zero.

Numerical Simulation: The finite-difference time-domain (FDTD) method is used to

calculate the scattering and absorption spectra of individual Bi_2S_3 nanostripes placed on the SiO_2 substrate. In the simulation, a total-field scattered-field (TFSF) source with the wavevector along *–z* axis is used to illuminate the Bi_2S_3 nanostripe. For simplicity, the cross section of the nanostripe is set to be square. The excitations with electric vector $\vec{E}$ perpendicular and parallel to the stripe are defined as *x*- and *y*-polarizations, respectively. The mesh grid is set to 1 nm at *x*, *y* and *z* directions. The real and imaginary parts of the refractive index of Bi_2S_3 are obtained from an ellipsometer (Figure S28). A constant of n = 1.46 is used for the substrate.

Note S2.

Definition of the key performance metrics of photodetectors

Responsivity (R) reflects the ability of photodetectors to generate photocurrent. It is extracted by the following formula

$$R = \frac{I_{\mathrm{Ph}}}{PA}, \tag{1}$$

where I_{Ph} is the photocurrent, which is calculated by $I_{\mathrm{Ph}} = I_{\mathrm{On}} - I_{\mathrm{Off}}$ (I_{On} is the channel current with illumination, and I_{Off} is the channel current in dark), P is the light power density, and A is the effective sensing area of photodetectors. EQE is defined as the efficiency of incident photons to generate free carriers collected by the electrodes, it can be extracted by

$$\mathrm{EQE} = \frac{hcI_{\mathrm{ph}}}{\lambda ePA} \times 100\% = \frac{hcR}{\lambda e} \times 100\%, \tag{2}$$

where h is the Planck constant, c is the speed of light, λ is the wavelength of incident light, and e is the elementary charge**.** Detectivity (D^*) is a performance metric evaluating the ability of photodetectors to identify weak signals of light. It is extracted by

$$D^* = \frac{R\sqrt{A}}{\sqrt{2eI_{\mathrm{Off}}}}. \tag{3}$$

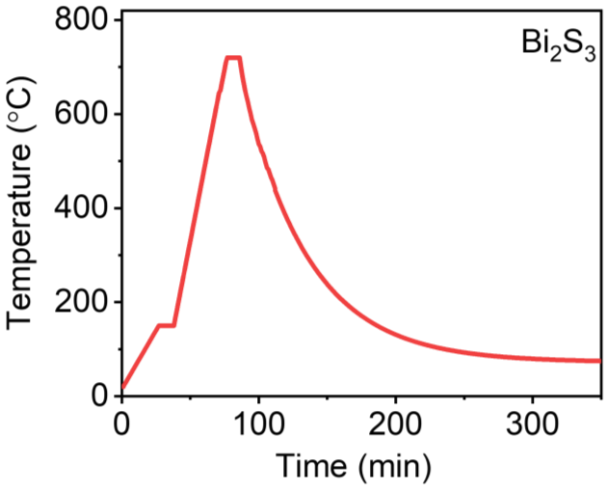

Figure S1. Furnace temperature as a function of time for the APCVD growth of Bi_2S_3 nanowires.

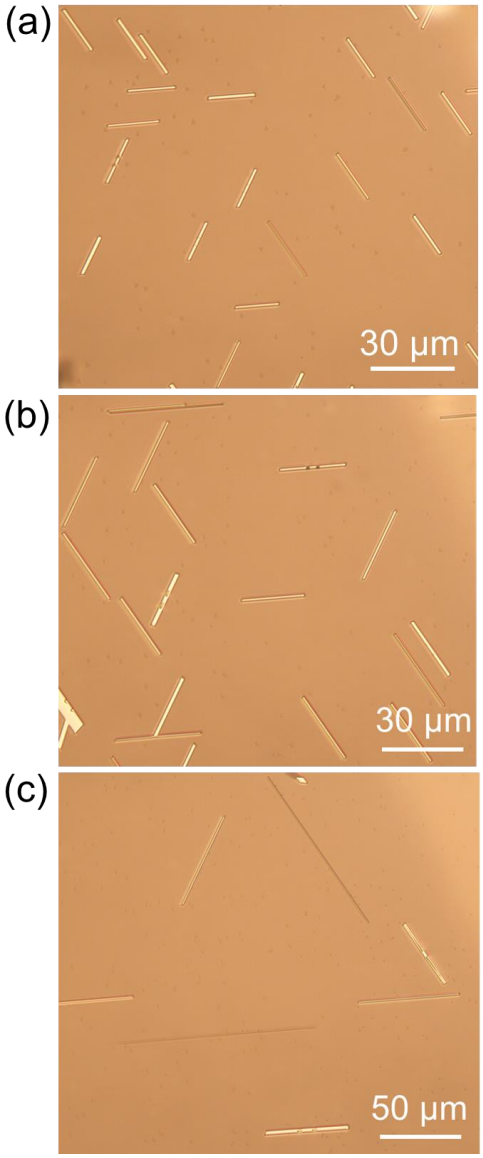

Figure S2. (a–c) Optical microscopy images of the APCVD-derived Bi_2S_3 nanowires on mica substrates.

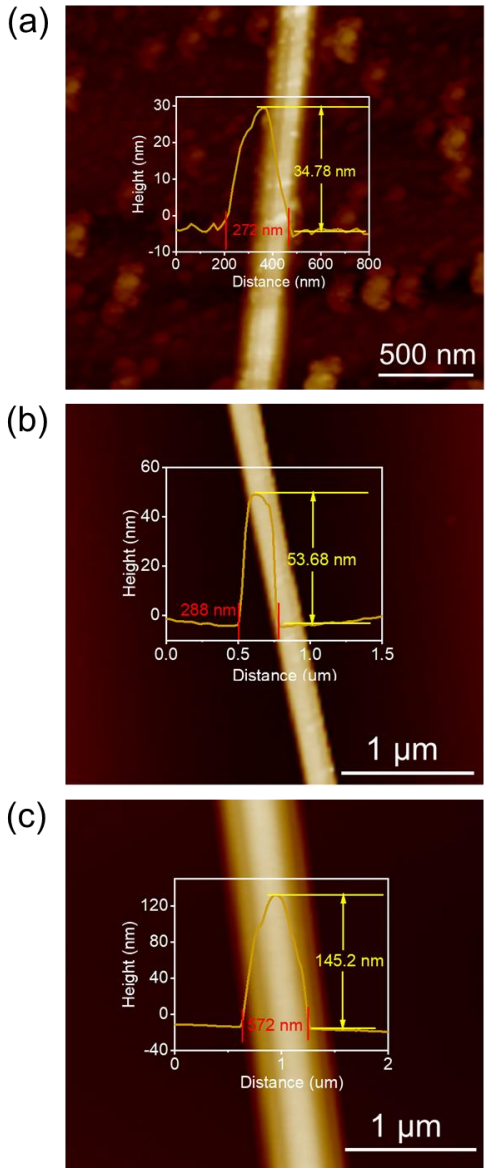

Figure S3. (a–c) AFM images of the APCVD-derived Bi_2S_3 nanowires. The insets present the corresponding height profiles across the nanowires.

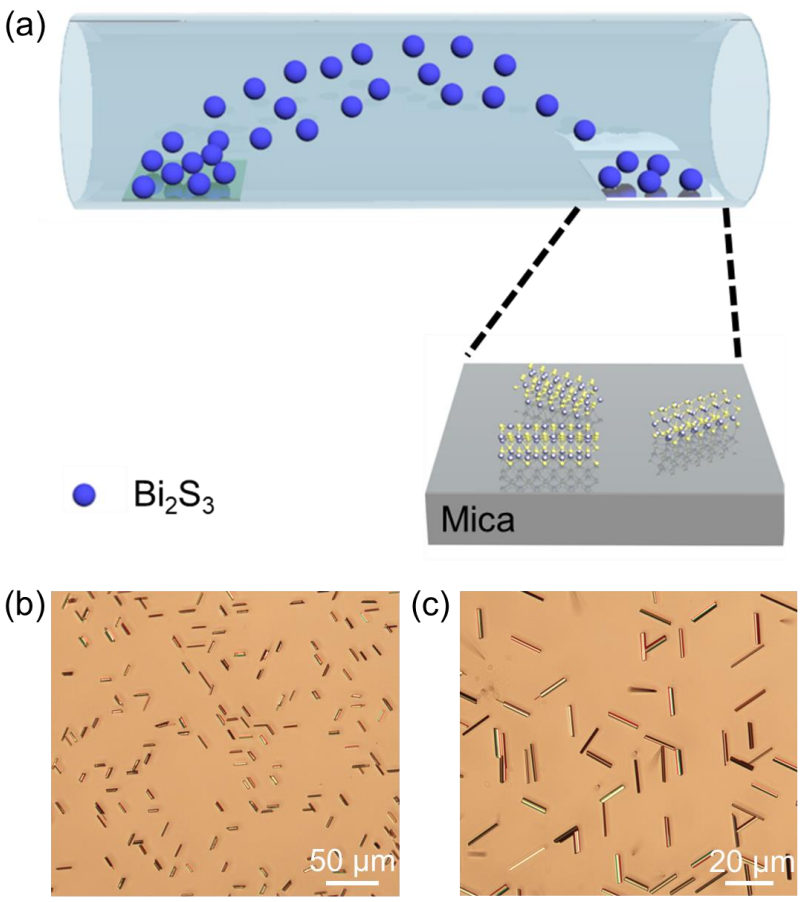

Figure S4. (a) Schematic diagram of the experimental configuration for the growth of Bi_2S_3 nanowires with a single Bi_2S_3 powder source precursor. (b–c) Optical microscopy images of the APCVD-derived Bi_2S_3 nanowires on mica substrates without using the S powder precursor. Overall, compared to the condition with the S powder precursor, the products are relatively short and thick.

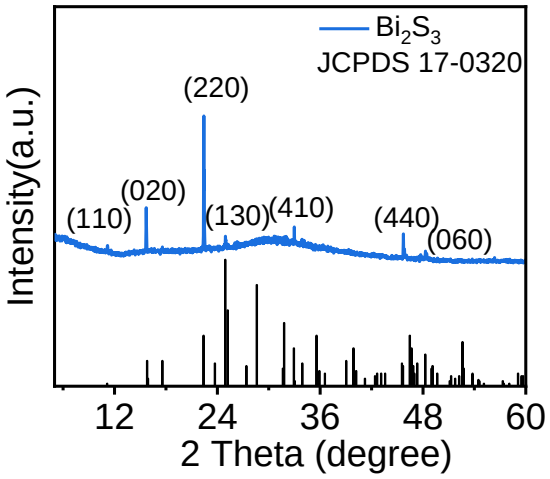

Figure S5. Typical XRD pattern of the APCVD-derived Bi_2S_3 nanowires on a SiO_2/Si substrate. The diffraction peaks centered at 11.16, 15.67, 22.37, 24.90, 32.96, 45.69, and 48.28 degrees can be well ascribed to the (110), (020), (220), (130), (410), (440), and (060) lattice planes, which are well consistent with the standard orthorhombic Bi_2S_3 (JCPDS No. 17-0320).

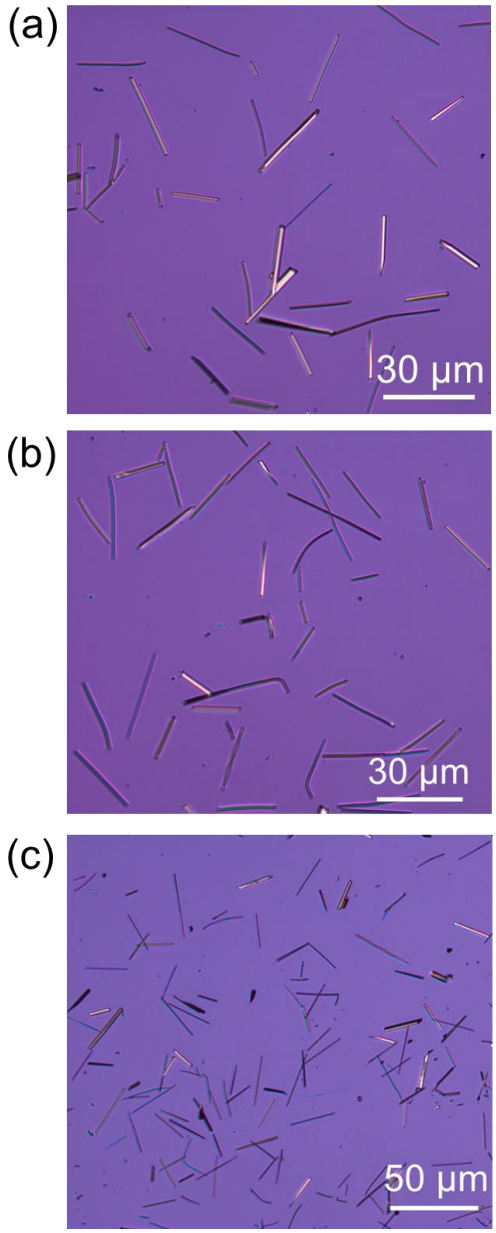

Figure S6. (a–c) Optical microscopy images of the APCVD-derived Bi_2S_3 nanowires grown on SiO_2/Si substrates. Overall, the spatial distribution of products on SiO_2/Si substrates is quite chaotic as compared to those on mica substrates. Meanwhile, a substantial portion of the nanowires suffer from obvious bending, which has also been observed in previous studies,[1, 2] indicating the formation of numerous lattice defects (such as dislocations, twins, *etc*.) during the growth process.

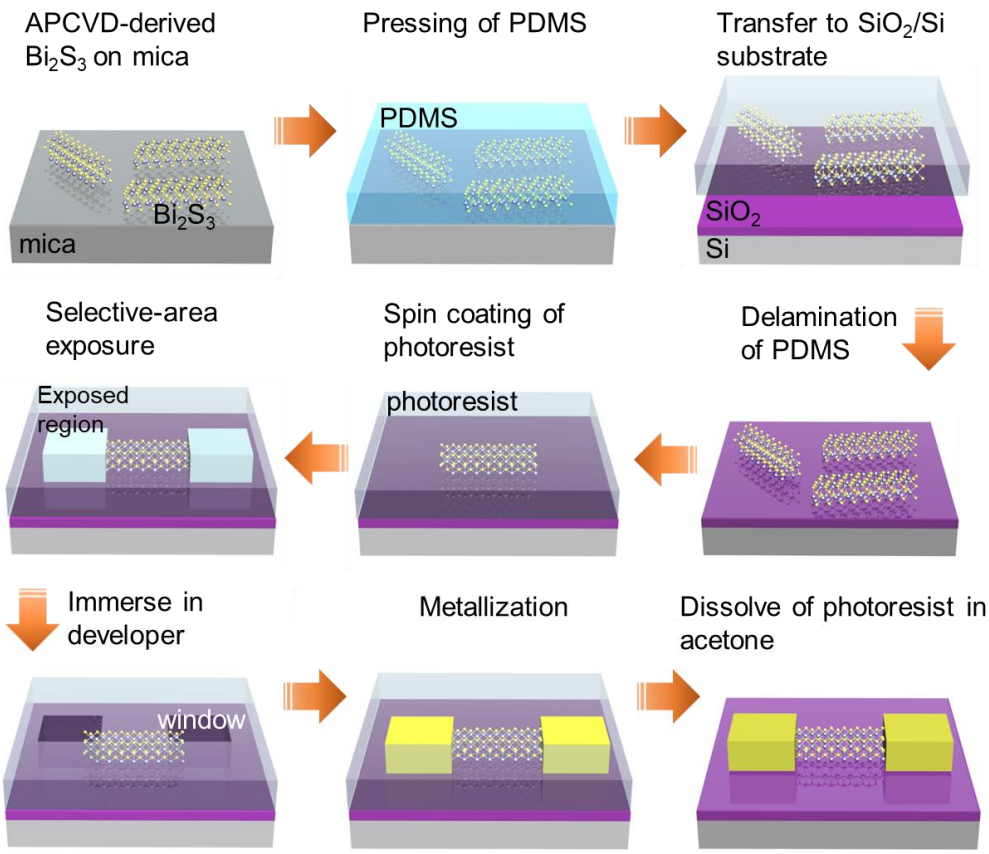

Figure S7. Fabrication procedures for constructing the Bi_2S_3 nanowire phototransistors.

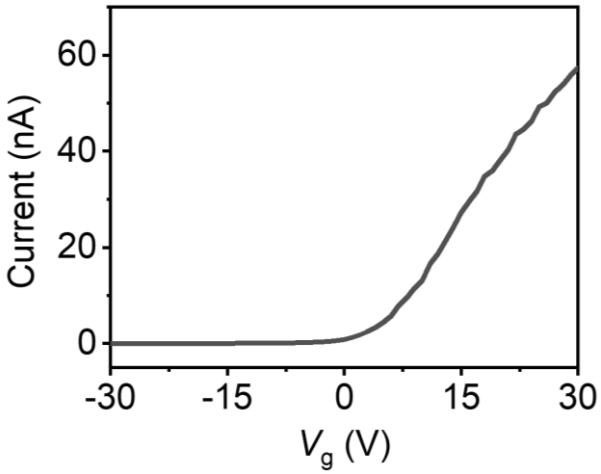

Figure S8. Transfer curve of a Bi_2S_3 field-effect transistor. Source-drain voltage: 1 V. The gate voltage is swept from −30 to 30 V.

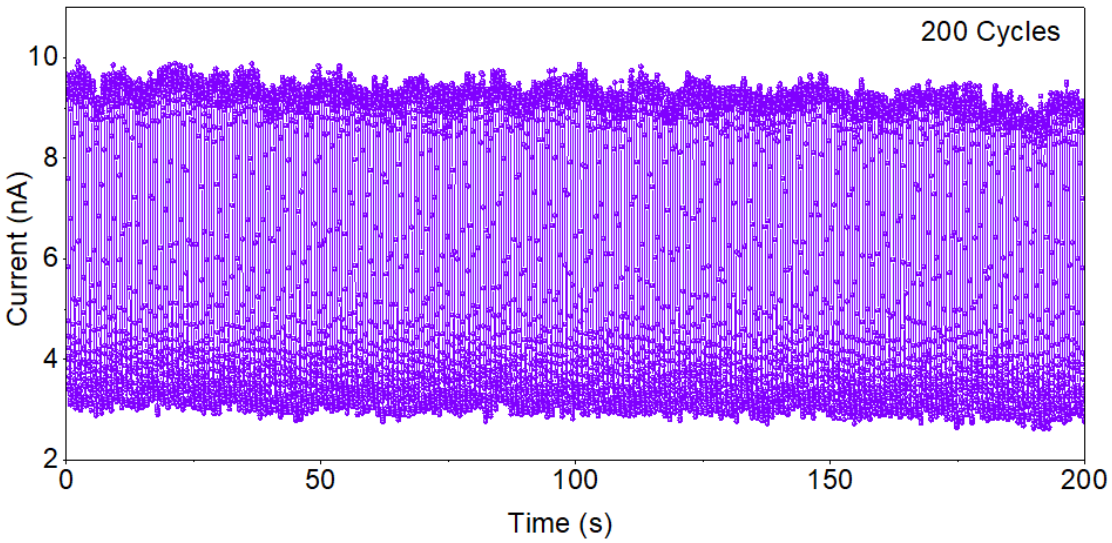

Figure S9. A typical photoswitching curve of a Bi_2S_3 photodetector over 200 on/off cycles.

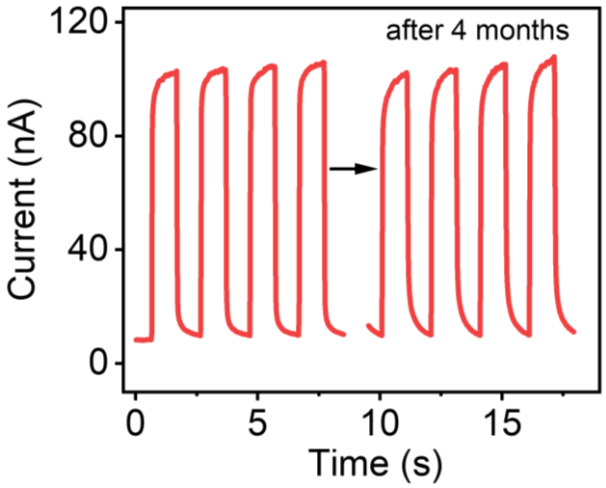

Figure S10. Photoswitching curves of a Bi_2S_3 photodetector right after fabrication (left) and after a four-months storage in air without any specific encapsulation strategies (right).

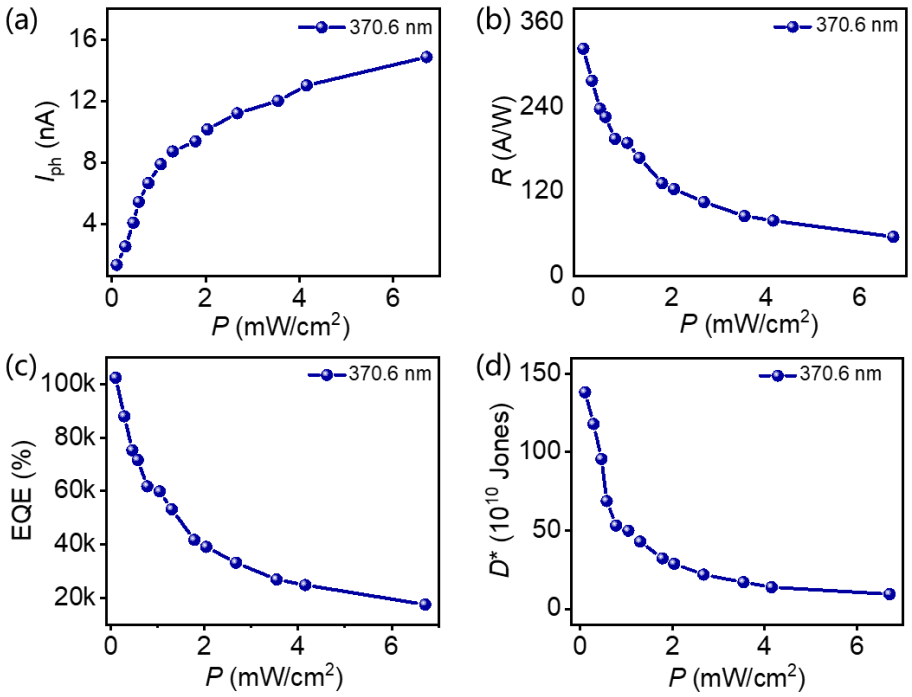

Figure S11. (a) Photocurrent, (b) responsivity, (c) EQE and (d) detectivity as a function of light power density of a Bi_2S_3 photodetector upon 370.6 nm illumination.

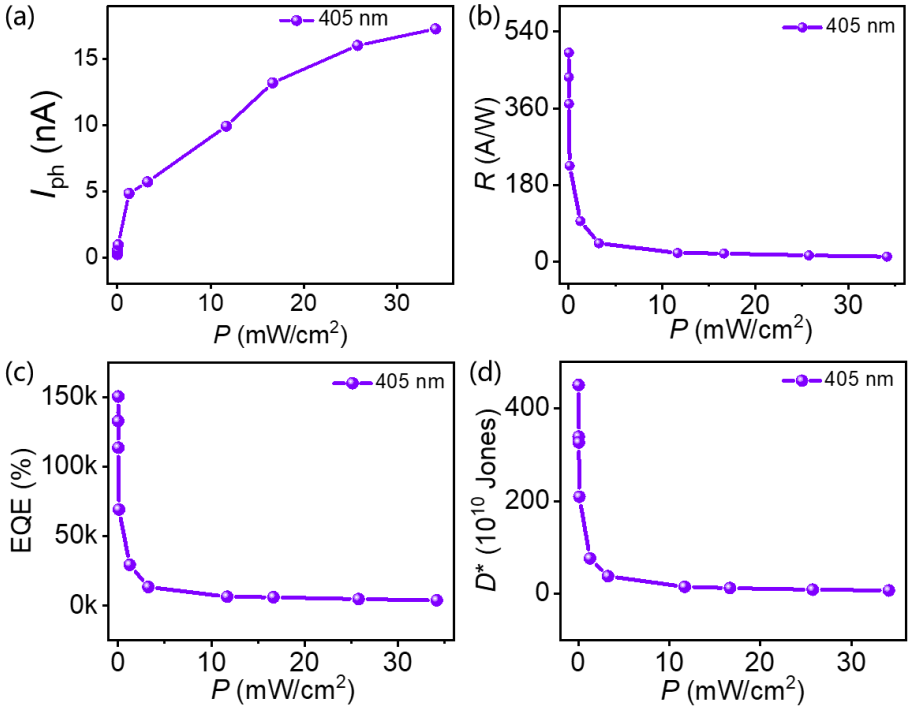

Figure S12. (a) Photocurrent, (b) responsivity, (c) EQE and (d) detectivity as a function of light power density of a Bi_2S_3 photodetector upon 405 nm illumination.

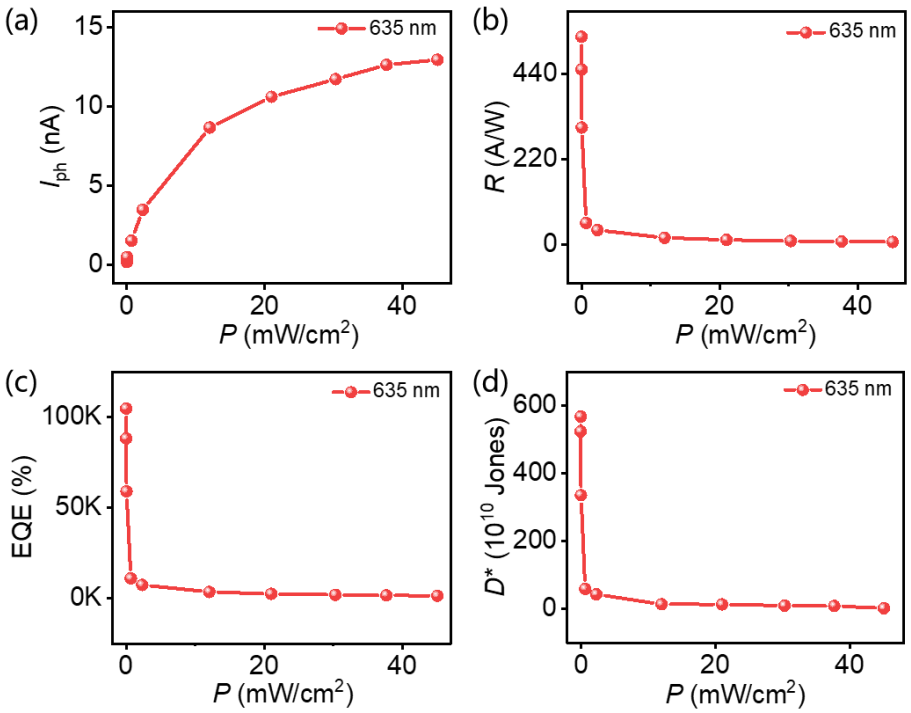

Figure S13. (a) Photocurrent, (b) responsivity, (c) EQE and (d) detectivity as a function of light power density of a Bi_2S_3 photodetector upon 635 nm illumination.

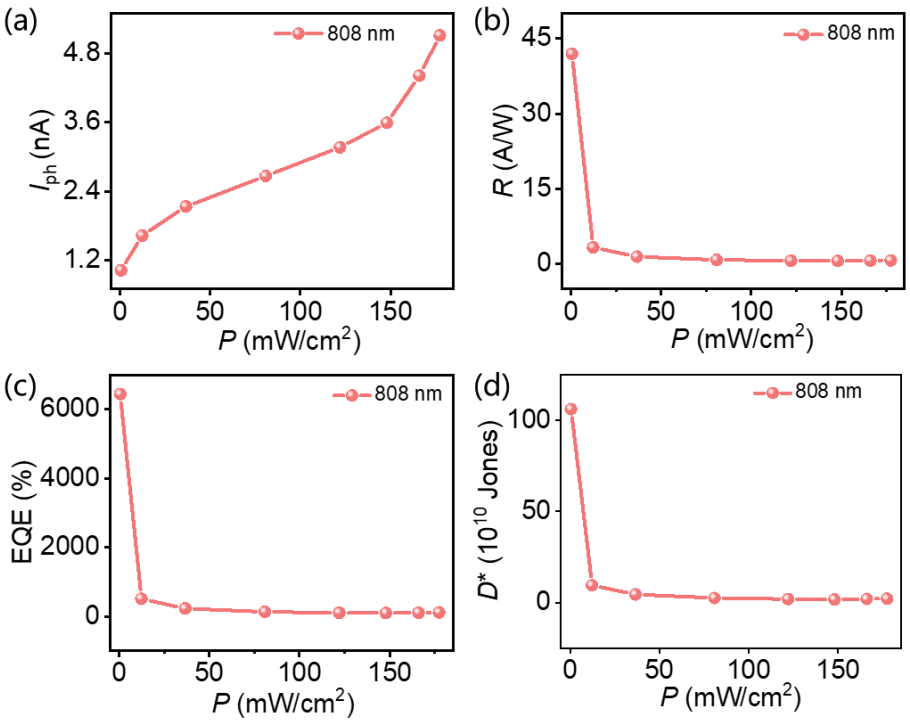

Figure S14. (a) Photocurrent, (b) responsivity, (c) EQE and (d) detectivity as a function of light power density of a Bi_2S_3 photodetector upon 808 nm illumination.

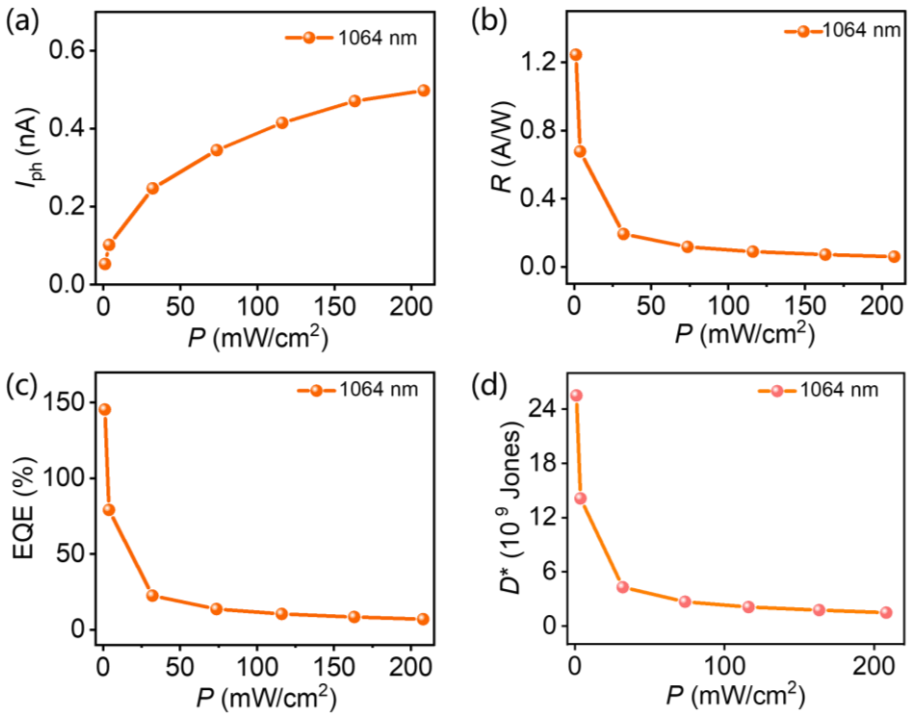

Figure S15. (a) Photocurrent, (b) responsivity, (c) EQE and (d) detectivity as a function of light power density of a Bi_2S_3 photodetector upon 1064 nm illumination.

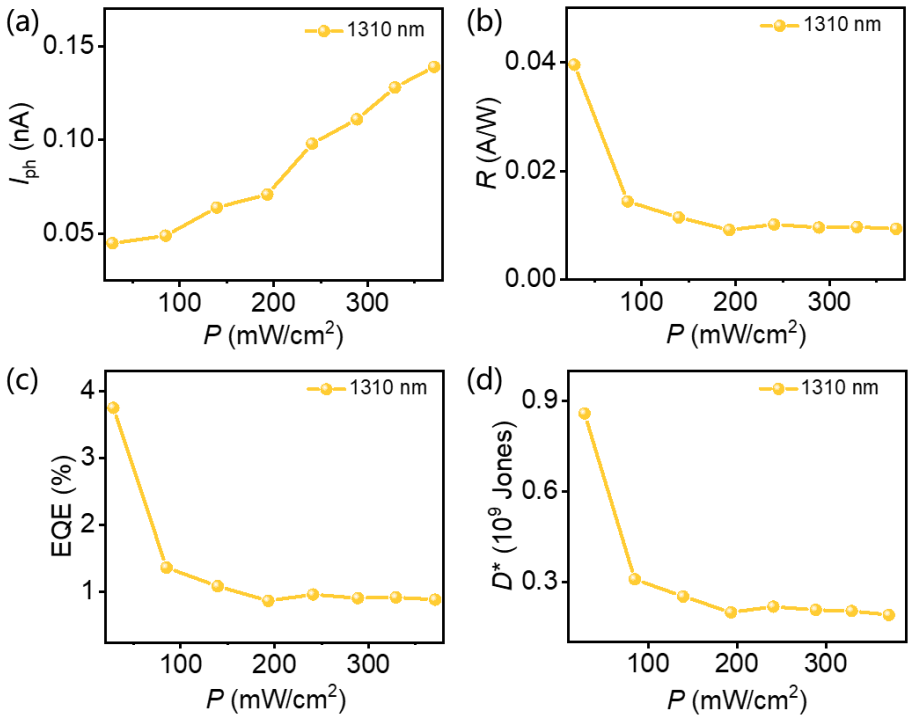

Figure S16. (a) Photocurrent, (b) responsivity, (c) EQE and (d) detectivity as a function of light power density of a Bi_2S_3 photodetector upon 1310 nm illumination.

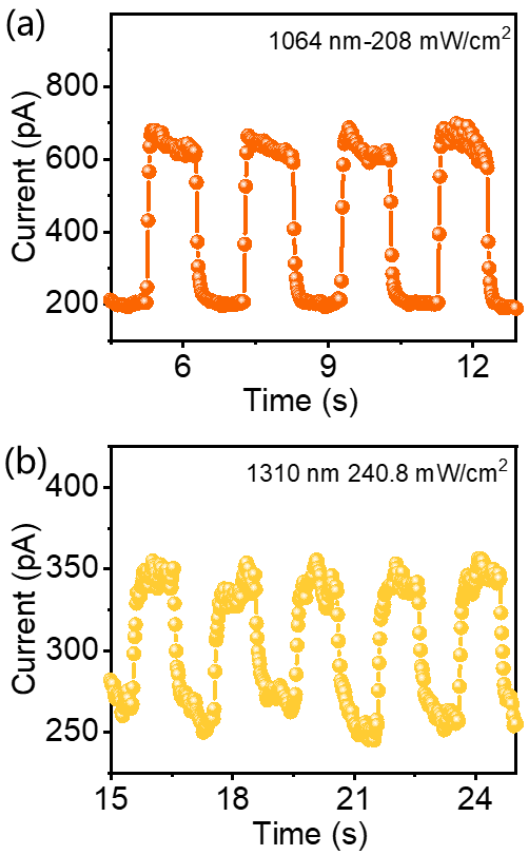

Figure S17. Photoswitching curves of an APCVD-derived Bi_2S_3 nanowire photodetector upon (a) 1064 and (b) 1310 nm illuminations.

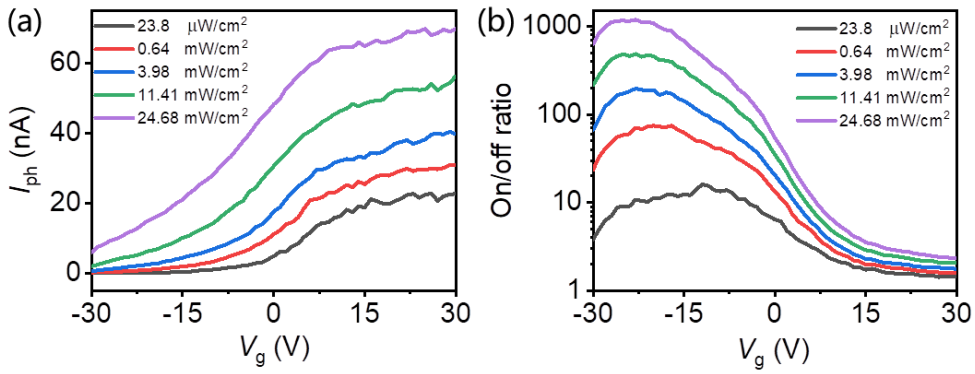

Figure S18. (a) Photocurrent and (b) on/off ratio as a function of back gate voltage of an APCVD-derived Bi_2S_3 nanowire photodetector upon illuminations with various light intensities.

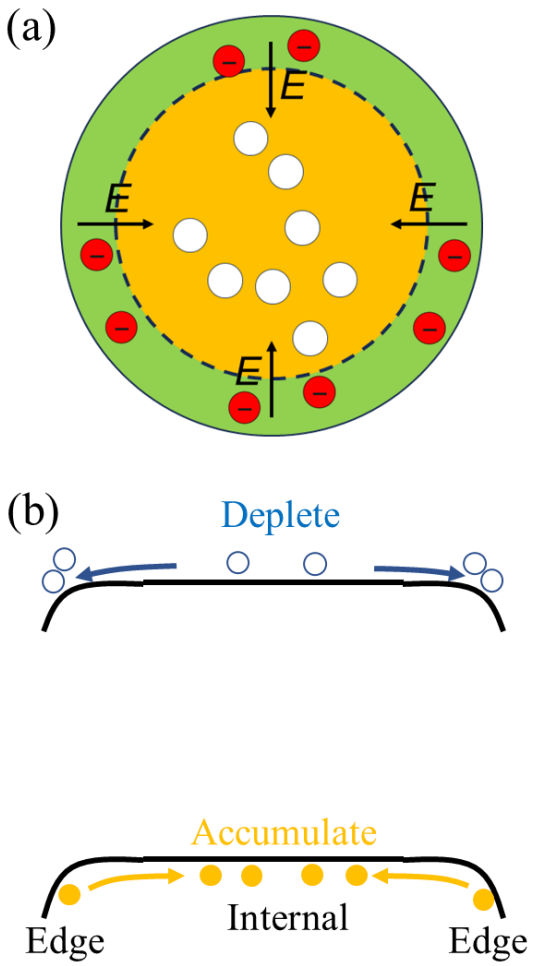

Figure S19. (a) Schematic diagram of the cross section of the Bi_2S_3 nanowire. The green region represents strained Bi_2S_3. The orange region represents pristine Bi_2S_3. The red balls represent electrons. The white balls represent holes. The arrows indicate axial built-in electric field. The dashed line represents the heterointerfaces. (b) Energy band diagram along the cross section of a Bi_2S_3 nanowire. The hollow balls represent photoexcited electrons, and the orange balls represent photoexcited holes.

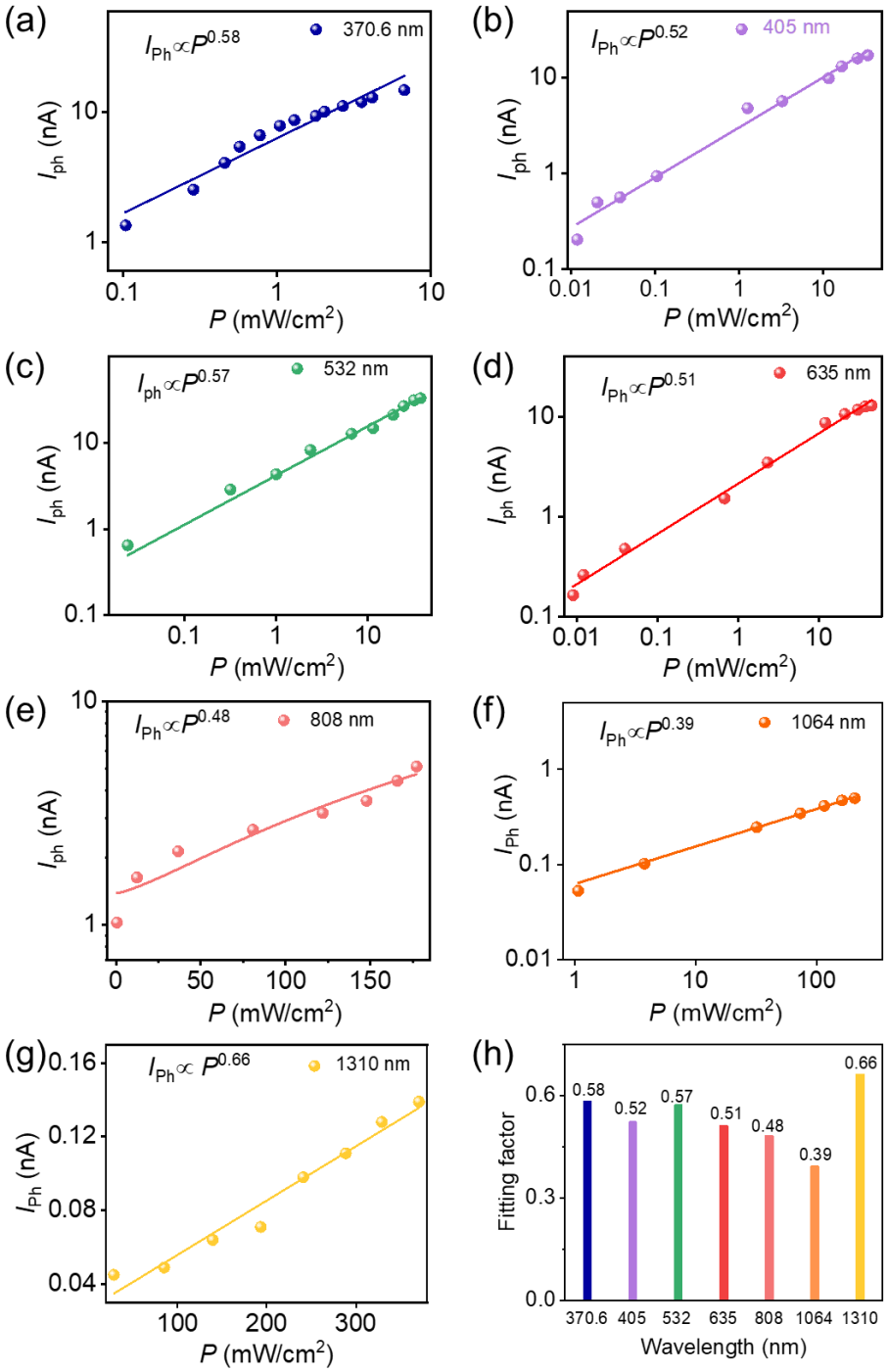

Figure S20. Light power density dependent photocurrent under (a) 370.6, (b) 405, (c) 532, (d) 635, (e) 808, (f) 1064, and (g) 1310 nm illuminations. The solid lines are the corresponding power law fittings. (h) A summary of the fitting factors of the power law fittings.

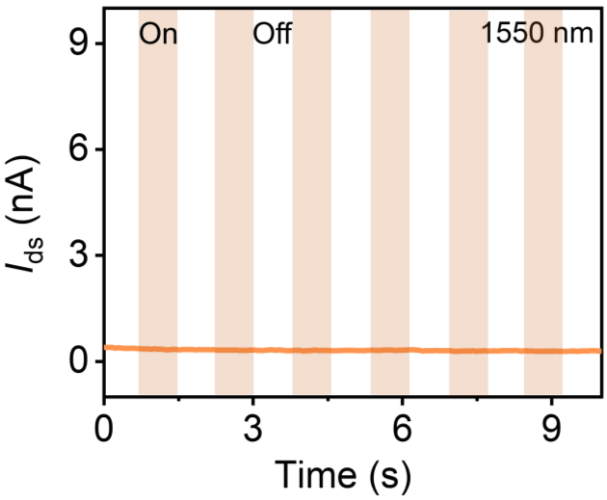

Figure S21. A typical *I-t* curve of a Bi_2S_3 nanowire photodetector upon periodic 1550 nm illumination. Power density: 43.98 mW/cm^2. The orange regions represent the illumination periods. Evidently, no discernible photoresponse can be identified.

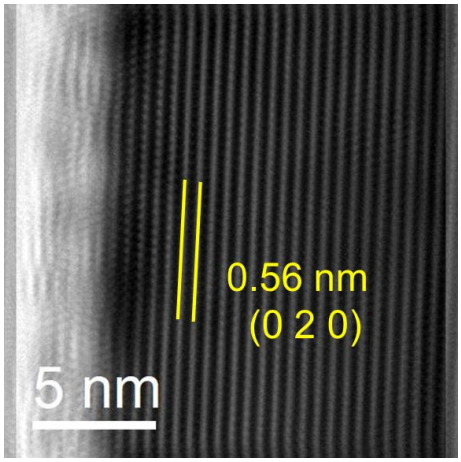

Figure S22. HRTEM image of the edge region of an APCVD-derived Bi_2S_3 nanowire. Scale bar: 5 nm. Evidently, compared to the internal crystal structure, the surface crystal structure exhibits obvious wrinkles, indicating the generation of strain.

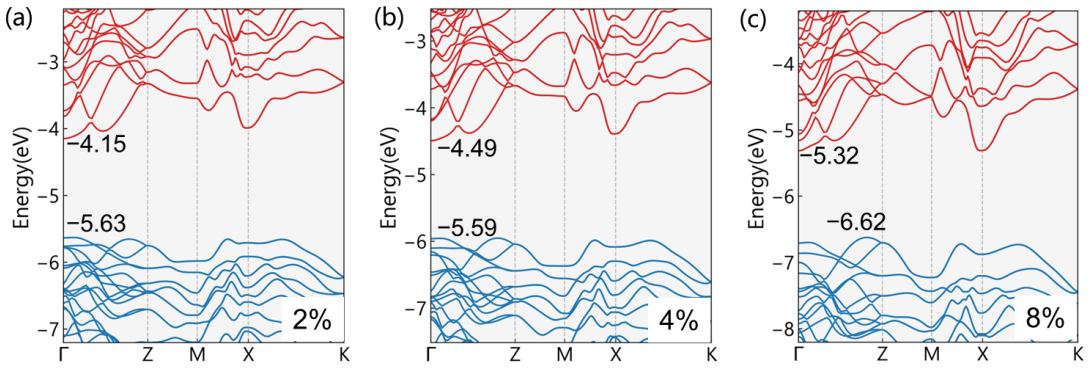

Figure S23. (a–c) Energy band diagrams of Bi_2S_3 upon 2%, 4%, and 8% strain, respectively.

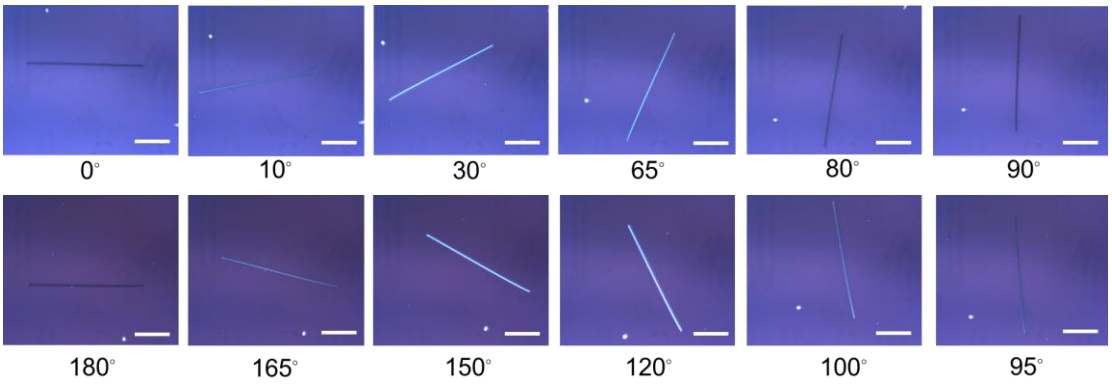

Figure S24. Polarization-resolved optical microscopy images of an APCVD-derived Bi_2S_3 nanowire transferred to a SiO_2/Si substrate. Scale bar: 50 μm. As the polarization angle varies from 0 to 180 degrees, the brightness changes periodically, which is consistent with the result of a previous study.[1] This measurement consolidates the highly anisotropic optical property of the Bi_2S_3 nanowire.

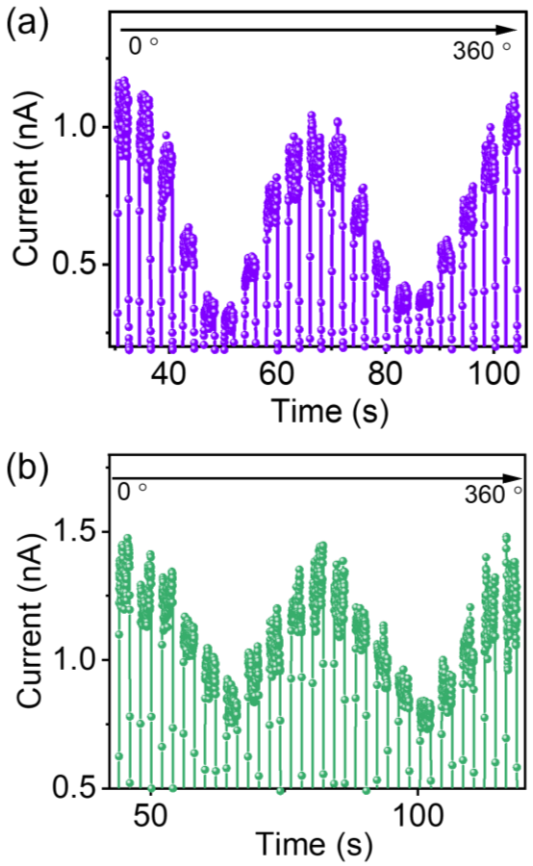

Figure S25. Photoswitching curves of a Bi_2S_3 photodetector upon (a) 405 and (b) 532 nm illuminations with changing polarization angle.

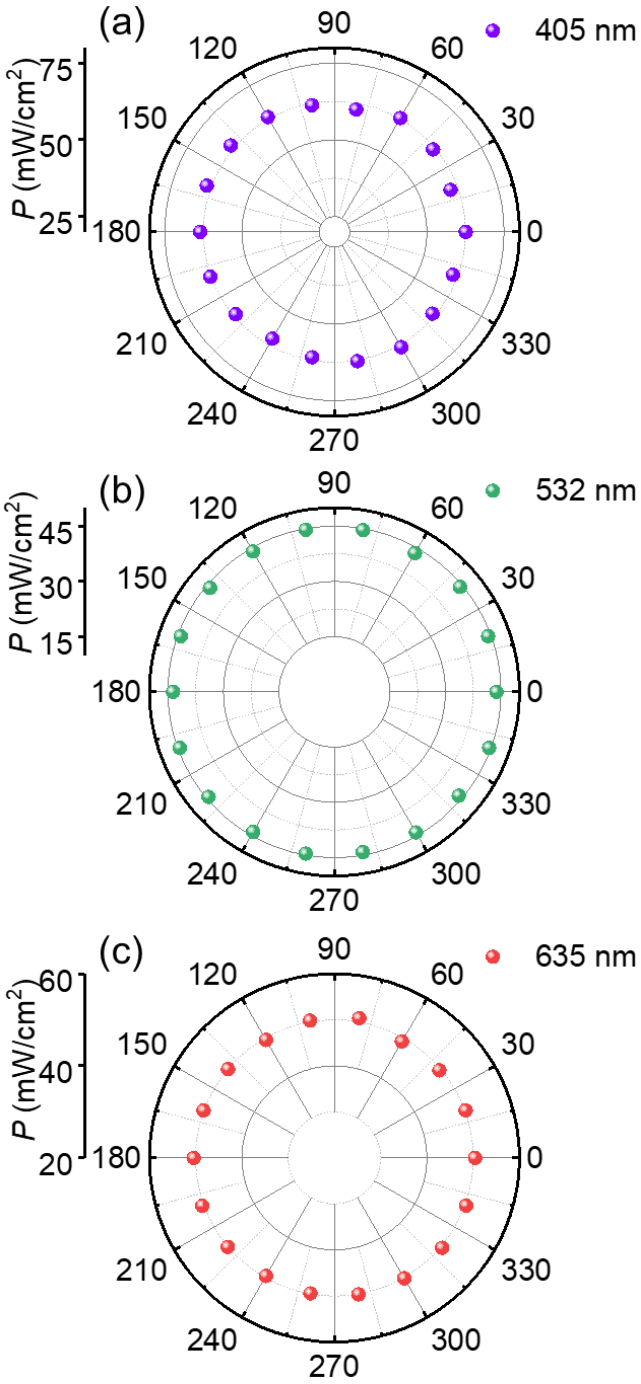

Figure S26. Polar plots of the power density of the (a) 405, (b) 532, and (c) 635 nm linearly polarized lights as a function of the polarization angle.

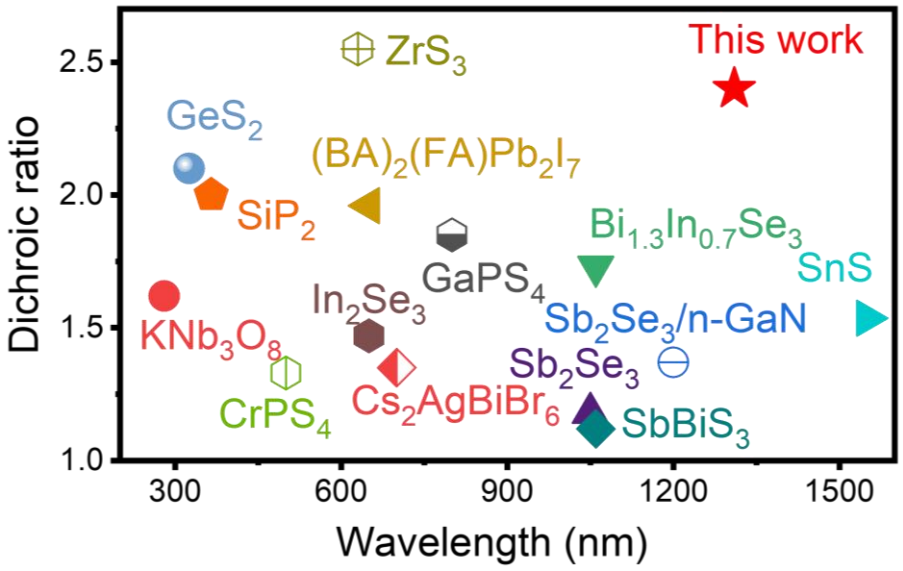

Figure S27. Comparison of the device properties of the APCVD-derived Bi_2S_3 photodetectors and the state-of-the-art low-dimensional material photodetectors.[3-16] The positions of the abscissa correspond to the maximum effective wavelengths of the devices.

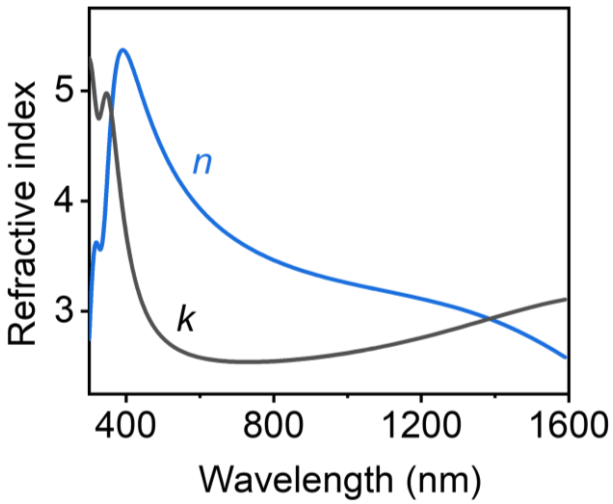

Figure S28. The real part (n, blue line) and imaginary part (k, black line) as a function of wavelength of the refractive index of Bi_2S_3.

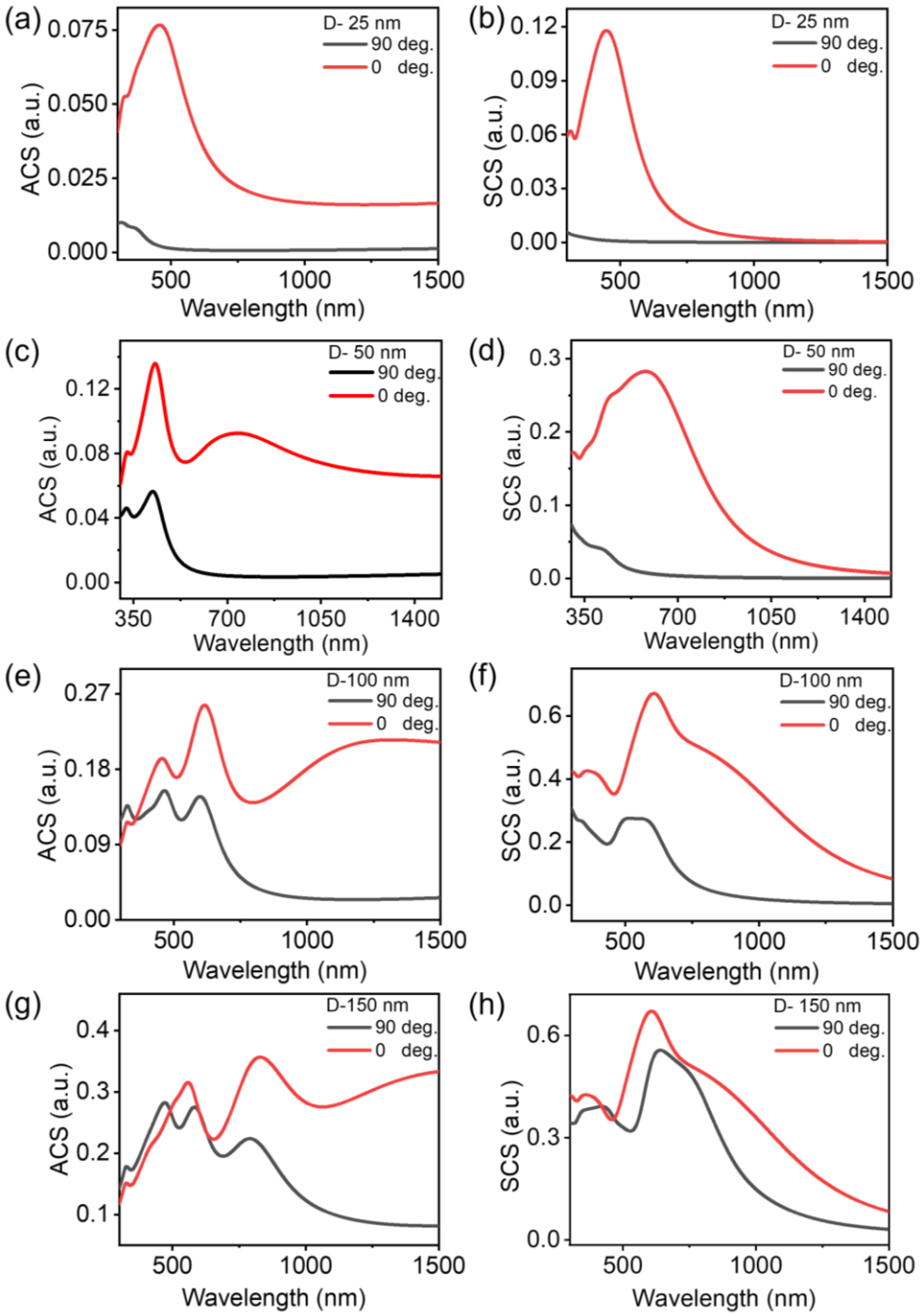

Figure S29. (a, c, e, g) ACS and (b, d, f, h) SCS of Bi_2S_3 nanowire under light illuminations with parallel polarization (red lines) and perpendicular polarization (black lines).

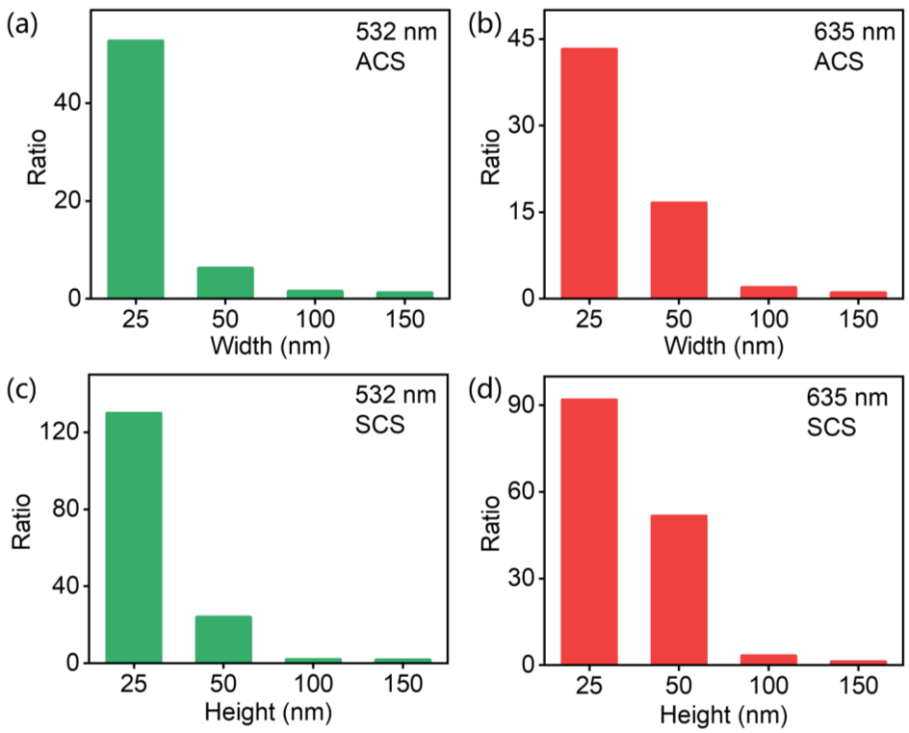

Figure S30. The ACS and SCS ratios of Bi_2S_3 nanowires with different widths/heights (25 nm, 50 nm, 100 nm, 150 nm) under parallel and perpendicular illuminations. (a) ACS ratio upon 532 nm illumination. (b) ACS ratio upon 635 nm illumination. (c) SCS ratio upon 532 nm illumination. (d) SCS ratio upon 635 nm illumination.

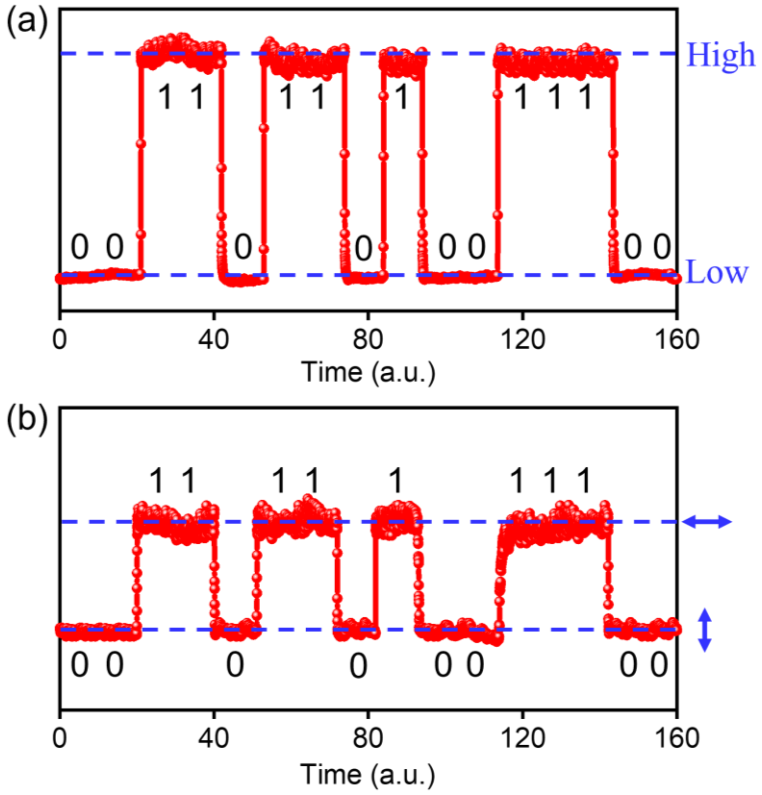

Figure S31. Information transmission of 0011011010011100 *via* merely (a) light intensity or (b) light polarization state, respectively. The "High" and "Low" represent the light intensity. The ↔ and ↕ represent the parallel and perpendicular polarization states, respectively.

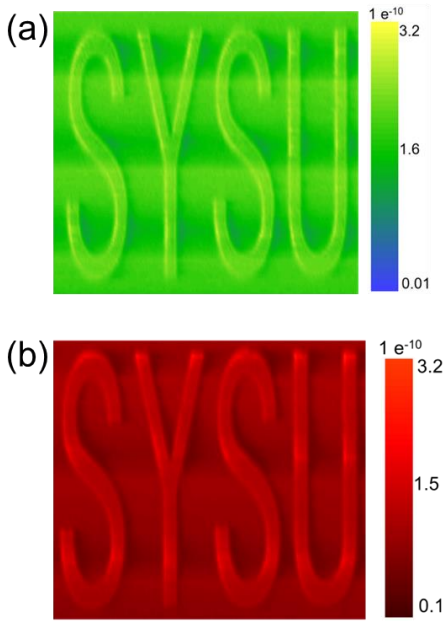

Figure S32. (a–b) The imaging results of an "SYSU" pattern by using 532 and 635 nm illuminations as the light sources, respectively.

Table S1. A summary of the performance metrics of the recently reported Bi_2S_3 based photodetectors.

Devices	R (A W^{-1})	D^* (Jones)	Rise/decay time	Effective wavelength range (nm)	Dichroic ratio	Ref.
Bi_2S_3 nanocrystal	44	1.5×10^{11}	23 ms/100 ms	400−900	N. A.[a)]	[17]
Bi_2S_3 nanosheet	4.4	2.1×10^{11}	10 μs/350 μs	400−800	N. A.	[18]
HGNs[b)]@Bi_2S_3 nanoribbon	1090	2.78×10^{13}	N. A.	350−700	N. A.	[19]
Bi_2S_3 nanoribbon	140	2.45×10^{12}	N. A.	350−700	N. A.	
Bi_2S_3 nanosheets	2.1×10^{-4}	3.75×10^{8}	100 ms/100 ms	300−800	N. A.	[20]
Bi_2S_3 nanowire	5233	1.8×10^{12}	21 μs/7.8 ms	500−980	N. A.	[21]
Bi_2S_3/$Bi_2S_{3-x}O_x$ nanowire	2908	1.01×10^{11}	0.47 ms/94 ms	325−1064	N. A.	[22]
Bi_2S_3 nanobelt	201	2.7×10^{10}	50 μs/200 μs	300−1000	N. A.	[23]
Bi_2S_3 nanosheet	8	N. A.	N. A.	400−850	N. A.	[24]
Bi_2S_3 nanowire	32	5×10^{11}	20 ms/10 ms	360−1064	1.9	[1]
Bi_2S_3 nanowires	4.21	1.64×10^{10}	12.25 ms/12.25 ms	400−830	1.79	[2]
Bi_2S_3 nanosheet	16.5	10^{10}	100 ms	785	N. A.	[25]
Fe-doped Bi_2S_3 nanocrystal	0.096	1.34×10^{10}	0.3 s/0.4 s	350−900	N. A.	[26]
Bi_2S_3 nanofibrous	0.002	2.89×10^{9}	47.1 ms/52.6 ms	940	N. A.	[27]
Bi_2S_3	**23760**	**3.68×10^{13}**	**1 ms/4.5 ms**	**370.6−1310**	**2.4**	**This work**

a) Not applicable. b) HGNs: hollow gold nanoparticles.

Table S2. A summary of the performance metrics of low-dimensional material photodetectors.

Devices	R (A W^{-1})	D* (Jones)	Rise/decay time	Effective wavelength range (nm)	Dichroic ratio	Ref.
KNb_3O_8 Nanobelt	30	5.95×10^{11}	2.5 s/1.8 s	230–280	1.62	[3]
Sb_2Se_3 Microbelt	0.18	1.1×10^{10}	144 ms/96 ms	400–1050	1.18	[4]
$Bi_{1.3}In_{0.7}Se_3$	241.3	1.18×10^{12}	980 ns/770 ns	254–1064	1.73	[5]
$SbBiS_3$	6.82	3.01×10^{9}	10 μs/94 μs	360–1064	1.12	[6]
$(BA)_2(FA)Pb_2I_7$	0.0248	3.34×10^{12}	240 μs/347 μs	377–637	1.96	[7]
SnS Nanosheets	310.5	N. A.	0.45 s/3.14 s	450–1550	1.536	[8]
In_2Se_3	1936	2.1×10^{13}	0.69 s/0.8 s	400–650	1.47	[9]
ZrS_3	0.23	4.24×10^{9}	N. A.	450–633	2.55	[10]
SiP_2	0.31	10^{12}	3 ms/3.5 ms	365	2	[11]
GeS_2	N. A.	N. A.	N. A.	325	2.1	[12]
$CrPS_4$	1.37×10^{-7}	5.82×10^{7}	2 s/2 s	350–500	1.33	[13]
$GaPS_4$	4.89	1.98×10^{12}	50 ms/50 ms	254–670	1.85	[14]
$Cs_2AgBiBr_6$	N. A.	N. A.	200 μs/400 μs	400–700	1.9	[15]
Sb_2Se_3/n-GaN	0.012	5×10^{10}	74 ms/75 ms	800–1200	1.37	[16]
Bi_2S_3	**23760**	**3.68×10^{13}**	**1 ms/4.5 ms**	**370.6–1310**	**2.4**	**This work**

References

1. W. Yang, J. Yang, K. Zhao, Q. Gao, L. Liu, Z. Zhou, S. Hou, X. Wang, G. Shen, X. Pang, Q. Xu and Z. Wei, *Adv. Sci.*, 2021, **8**, 2100075.
2. H. Wang, R. Liu, S. Zhang, Y. Wang, H. Luo, X. Sun, Y. Ren and W. Lei, *Opt. Mater.*, 2022, **134**, 113174.
3. Y. Ping, H. Long, H. Liu, C. Chen, N. Zhang, H. Jing, J. Lu, Y. Zhao, Z. Yang, W. Li, F. Ma, X. Fang, Z. Wei and H. Xu, *Adv. Funct. Mater.*, 2022, **32**, 2111673.
4. P. Wan, M. Jiang, L. Su, S. Xia, Y. Wei, T. Xu, Y. Liu, D. Shi, X. Fang and C. Kan, *Adv. Funct. Mater.*, 2022, **32**, 2207688.
5. F. Zhang, Y. Yu, Z. Mo, L. Huang, Q. Xia, B. Li, M. Zhong and J. He, *Nano Res.*, 2022, **15**, 8451–8457.
6. W. Yang, T. Xiong, Y. Y. Liu, J. Yang, Q. Xu and Z. Wei, *Small Struct.*, 2022, **3**, 2200061.
7. Z. Xu, X. Dong, L. Wang, H. Wu, Y. Liu, J. Luo, M. Hong and L. Li, *J. Am. Chem. Soc.*, 2023, **145**, 1524–1529.
8. Y. Cui, Z. Zhou, X. Wang, X. Wang, Z. Ren, L. Pan and J. Yang, *Nano Res.*, 2021, **14**, 2224–2230.
9. S. Wang, Z. Yang, D. Wang, C. Tan, L. Yang and Z. Wang, *ACS Appl. Mater. Interfaces*, 2023, **15**, 3357–3364.
10. X. Wang, K. Wu, M. Blei, Y. Wang, L. Pan, K. Zhao, C. Shan, M. Lei, Y. Cui, B. Chen, D. Wright, W. Hu, S. Tongay and Z. Wei, *Adv. Electron. Mater.*, 2019, **5**, 1900419.
11. Z. Wang, P. Luo, B. Han, X. Zhang, S. Zhao, S. Wang, X. Chen, L. Wei, S. Yang, X. Zhou, S. Wang, X. Tao and T. Zhai, *ACS Nano*, 2021, **15**, 20442–20452.
12. Y. Yang, S. C. Liu, X. Wang, Z. Li, Y. Zhang, G. Zhang, D. J. Xue and J. S. Hu, *Adv. Funct. Mater.*, 2019, **29**, 1900411.
13. H. Zhang, Y. Li, X. Hu, J. Xu, L. Chen, G. Li, S. Yin, J. Chen, C. Tan, X. Kan and L. Li, *Appl. Phys. Lett.*, 2021, **119**, 171102.

14. Y. Yan, J. Yang, J. Du, X. Zhang, Y. Y. Liu, C. Xia and Z. Wei, *Adv. Mater.*, 2021, **33**, 2008761.
15. Y. Li, T. Yang, Z. Xu, X. Liu, X. Huang, S. Han, Y. Liu, M. Li, J. Luo and Z. Sun, *Angew. Chem., Int. Ed.*, 2020, **59**, 3429–3433.
16. P. Wan, M. Jiang, Y. Wei, T. Xu, Y. Liu, S. Xia, L. Su, D. Shi, X. Fang and C. Kan, *Adv. Opt. Mater.*, 2023, **11**, 2202080.
17. G. Konstantatos, L. Levina, J. Tang and E. H. Sargent, *Nano Lett.*, 2008, **8**, 4002–4006.
18. G. Chen, Y. Yu, K. Zheng, T. Ding, W. Wang, Y. Jiang and Q. Yang, *Small*, 2015, **11**, 2848–2855.
19. F. X. Liang, C. W. Ge, T. F. Zhang, W. J. Xie, D. Y. Zhang, Y. F. Zou, K. Zheng and L. B. Luo, *Nanophotonics*, 2017, **6**, 494–501.
20. W. Huang, C. Xing, Y. Wang, Z. Li, L. Wu, D. Ma, X. Dai, Y. Xiang, J. Li, D. Fan and H. Zhang, *Nanoscale*, 2018, **10**, 2404–2412.
21. X. Xu, C. Fan, Y. Wang, Z. Qi, B. Dai, H. Jiang, S. Wang and Q. Zhang, *Phys. Status Solidi RRL*, 2020, **14**, 2000384.
22. Y. Liu, P. Chen, G. Dai, W. Su, Y. Sun, J. Hou, N. Zhang, G. Zhao, Y. Fang and N. Dai, *Phys. E*, 2020, **120**, 114041.
23. J. Xu, H. Li, S. Fang, K. Jiang, H. Yao, F. Fang, F. Chen, Y. Wang and Y. Shi, *J. Mater. Chem. C*, 2020, **8**, 2102–2108.
24. K. A. Messalea, A. Zavabeti, M. Mohiuddin, N. Syed, A. Jannat, P. Atkin, T. Ahmed, S. Walia, C. F. McConville, K. Kalantar-Zadeh, N. Mahmood, K. Khoshmanesh and T. Daeneke, *Adv. Mater. Interfaces*, 2020, **7**, 2001131.
25. B. Chitara, B. S. C. Kolli and F. Yan, *Chem. Phys. Lett.*, 2022, **804**, 139876.
26. S. Rajeswari, M. M. Ibrahim, I. L. Poul Raj, J. Hakami, M. Imran, S. AlFaify and M. Shkir, *Sens. Actuators, A*, 2022, **345**, 113759.
27. P. Rong, S. Gao, S. Ren, H. Lu, J. Yan, L. Li, M. Zhang, Y. Han, S. Jiao and J. Wang, *Adv. Funct. Mater.*, 2023, **33**, 2300159.